

Miniature Wireless Magnetoelastic Resonant Motor With Frequency Selectable Bidirectional Rotation

Jun Tang, Scott R. Green, and Yogesh B. Gianchandani, *Fellow, IEEE*

Abstract—This paper presents the analysis, fabrication, and experimental results of wirelessly actuated chip-scale rotary motors. Two designs are described. Design M is actuated by a ϕ 8-mm magnetoelastic stator lithographically micromachined from Metglas 2826MB-bulk-foil with 25 μ m thickness. It operates at a resonant frequency of 11.35 kHz while 3-Oe dc and 2-Oe amplitude ac magnetic fields are applied. The measured rotation speed, start torque, calculated driving step size, and payload are 44 r/min, 2 nN · m, \approx 23 mdeg, and 9 mg, respectively. Design S uses a stator that is a sandwich of Si (ϕ 8 mm diameter and 65 μ m thickness) and magnetoelastic foil (ϕ 8 mm diameter and 25 μ m thickness) to tailor the stiffness. The typical resonant frequencies of clockwise (CW) mode and counterclockwise (CCW) mode are 6.1 and 7.9 kHz, respectively. The CCW mode provides a rotation rate of about 100 r/min, start torque of 30 nN · m, and driving step size of 74 mdeg while 8-Oe dc and 6-Oe amplitude ac magnetic fields are applied. Bidirectional rotation is realized by switching the applied frequency, thereby exciting the stator in a slightly different mode shape. Design S shows at least 43-mg payload capability. [2012-0207]

Index Terms—Magnetostrictivity, Metglas, photochemical machining (PCM), transient liquid phase bonding.

I. INTRODUCTION

CHIP-SCALE rotary motors have been of interest since the 1980s. There are a number of microsystem applications that would benefit from rotary micromotors, including defense, robotics, aerospace, laboratory automation, medical, and so on. One interesting example application involves the integration of a rotary micromotor with a MEMS gyro. The controlled rotational input can be used for *in situ* recalibration of signal drift from the gyro, rather than requiring the gyro to be taken out of service for calibration. Another possible application for a wirelessly actuated miniature motor is to provide propulsive force for microbots in cavities and ducts. Similar robotic technology can potentially conduct *in situ* monitoring and repair of large-scale complex machines, such as engines, eliminating the need for disassembly.

Manuscript received July 18, 2012; revised December 3, 2012; accepted January 14, 2013. Date of publication February 22, 2013; date of current version May 29, 2013. Subject Editor D.-I. Cho.

The authors are with the Center for Wireless Integrated MicroSensing and Systems (WIMS²), University of Michigan, Ann Arbor, MI 48109-2125 USA (e-mail: juntang@umich.edu; greensr@umich.edu; yogesh@umich.edu).

Color versions of one or more of the figures in this paper are available online at <http://ieeexplore.ieee.org>.

Digital Object Identifier 10.1109/JMEMS.2013.2242253

Rotary motor actuation methods have included electrostatic, electromagnetic, piezoelectric, thermal, and so on. Electrostatic motors [1], [2] are considered as one of the milestones in MEMS history. These motors usually can operate at very high rotation rate and are compatible with IC processes, but packaging requirements, output torque, and payload capacity limit applicability. In recent years, there have been improvements in torque and payload capacity by utilizing miniature ball bearings [3] and liquid bearing [4] systems. Macroscale electromagnetic motors are very mature, but efforts toward their miniaturization have resulted in landmark accomplishments for the microsystem research community [5]–[8]. Relative to other technologies, these motors typically offer high rotation rate and torque, but integration of coils requires careful consideration. Another successful and well-studied technology is piezoelectric micromotors [9]–[14]. Piezoelectric ultrasonic motors usually have a piezoelectric stator resonating at a high frequency. In each cycle, the rotor is pushed by a small tangential step. These motors usually have high payload, high stall torque, and high angular resolution. Thermally actuated rotary motors [15] can be used for applications requiring large forces. In this paper, another option for chip-scale rotary motors—magnetoelastic actuation—is investigated.

Magnetoelastic coupling represents the interaction between the material conditions of strain, stress, and magnetization. Magnetoelastic materials exhibit strains under an external magnetic field due to the field-directed rotation and alignment of tightly coupled, elongated structural, and magnetic domains in the materials. The strain induces stress in the material, which, in turn, alters the magnetization. When excited with an oscillatory field, these two simultaneously existing effects make magnetoelastic materials attractive for wireless resonant sensing. Various magnetoelastic sensing systems have been studied for pressure, temperature, liquid viscosity and density, fluid flow rate, pH, glucose, Young's modulus, stent occlusion, etc. [16]. Utilizing magnetoelastic material for actuation in miniature and microscale systems remains an open challenge. Magnetoelastic actuators can operate by mechanically resonating in response to an alternating magnetic field. The resonant motion is used to drive movement of other parts of the system. The use of magnetoelastic transduction enables wireless actuation, which simplifies device architecture and allows for remote operation. The transduction method exhibits relatively high payload carrying capacity. It also offers noise immunity due to resonant operation.

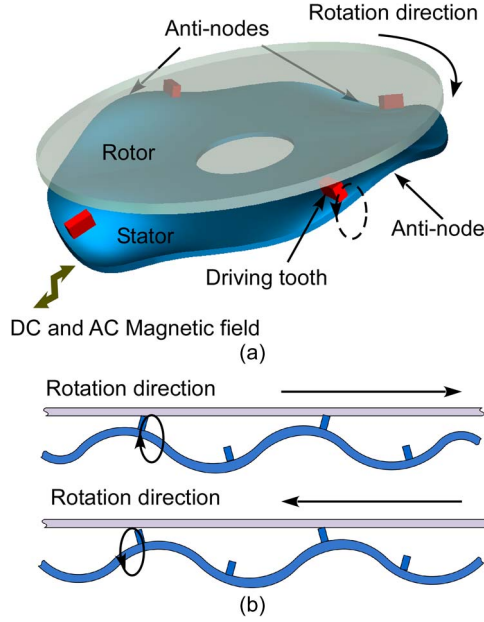


Fig. 1. Wireless magnetoelastic resonant rotary motor operation concept. (a) Standing wave in stator. (b) Bidirectional rotation operation method.

This paper describes two types of magnetoelastic rotary motors: in design M,¹ the motor is actuated by a magnetoelastic bulk foil stator; in design S, the motor is driven by a stator that uses a sandwich of Si and magnetoelastic foil. Both designs successfully demonstrate the wireless magnetoelastic rotary actuation method. Furthermore, bidirectional rotation of the design S motor is achieved by exciting the stator vibration in slightly different mode shapes. Section II provides a theory of motor operation, simulation of the magnetoelastic rotary actuation method, and geometrical design of the two prototypes. Section III details the fabrication process of the motors. Section IV describes the experimental setup and preliminary results. Section V discusses the advantages of the wireless rotary actuation method, performance comparison of the two designs, and performance improvement plans. Section VI provides the conclusion.

II. DESIGN AND MODELING

A. Theory

The rotary actuation mechanism in this effort is similar to that for piezoelectric ultrasonic rotary motors [9]. A vibratory wave, which could be either standing wave or travelling wave, is generated in the stator. In this case, the vibratory micromotion is a standing flexural resonant wave and is generated magnetoelastically. The resulting vibratory mode shape of the stator has antinodes at which maximal out-of-plane deflection occurs. Teeth are located on the stator such that they are slightly offset from the antinodes, resulting in elliptical motion of the teeth tip and a contact force with a tangential component that causes the rotor to rotate (Fig. 1). By selecting resonant frequency of different mode shapes of the stator, bidirectional rotation can be achieved. A rotor, which can contain other microsystem components, is then stacked above the stator.

¹Portions of this paper have appeared in conference abstract form in [17].

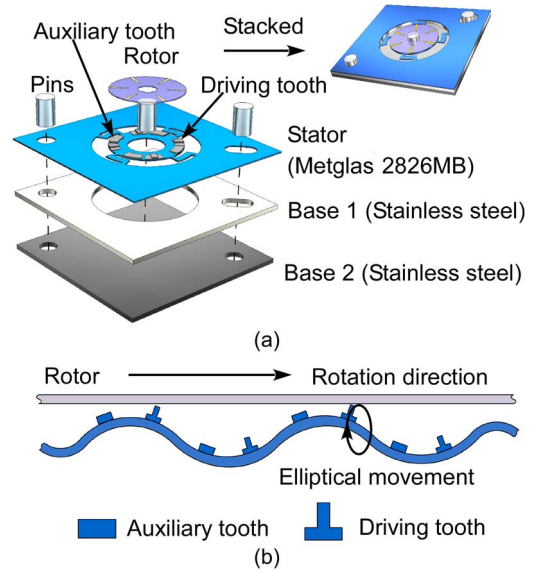


Fig. 2. (a) Schematic of design M geometry. (b) Customized teeth design. In design M, the stator is fabricated from magnetoelastic metal foil alone.

Singular magnetoelastic material, which can either be the vibrating stator itself or the actuator for the stator, can be wirelessly driven by magnetic fields. The deformation is substantially enhanced if a proper dc magnetic field is superimposed on the ac magnetic field. Thus, both dc and ac magnetic fields are required for rotary motor wireless actuation [18].

B. Modeling

A custom magnetomechanical harmonic finite-element technique [18] is used to estimate modal displacements, shapes, and frequencies for the magnetoelastic material. Although magnetoelastic materials are generally nonlinear, it is appropriate to use linearized constitutive equations describing the coupling between flux, field strength, stress, and strain in a magnetostrictive material

$$\vec{\sigma} = [C]\vec{\varepsilon} - \frac{[C][d]^T}{\mu_0\mu_r}\vec{B} \quad (1)$$

$$\vec{H} = -\frac{[d][C]}{\mu_0\mu_r}\vec{\varepsilon} + \frac{1}{\mu_0\mu_r}\vec{B} \quad (2)$$

where σ is the stress vector, C is the stiffness matrix, ε is the strain, d is the magnetostrictivity matrix, B is the magnetic flux density vector, H is the field strength vector, μ_0 is the permeability of free space, and μ_r is the relative permeability. Equations (1) and (2) are implemented in this paper by utilizing COMSOL Multiphysics and coupled time-harmonic induction current and stress–strain frequency response modes. A detailed look at a finite-element analysis (FEA) implementation for magnetostrictive materials is presented in [19]; the approach used in this work is modified for application to resonant actuators. In this paper, two types of magnetoelastic rotary motor, namely, design M and design S, are modeled and investigated.

C. Design M

The design M motor consists of a magnetoelastic material—Metglas 2826MB stator—and two stainless steel bases

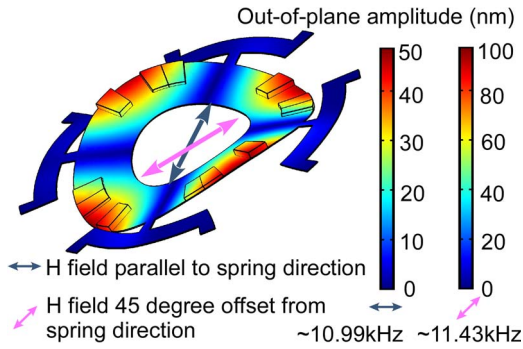


Fig. 3. FEA simulation results of the frequency response of the bulk-magnetoelastic-foil stator of design M.

[Fig. 2(a)]. The stacked architecture is modular, which significantly simplifies the fabrication process. Each layer can be easily fabricated by utilizing photochemical machining (PCM) process, as described in the fabrication section. Alignment pins ensure reasonable assembly accuracy. Two stainless steel bases provide a recess allowing stator vibration and initial positions for alignment pins and a hub. The ring-shaped stator is suspended with four crab-leg springs, which are stiff in the rotational direction but flexible in the out-of-plane direction—preventing stator rotation during rotor actuation and allowing large vertical deformation.

For a stator fabricated solely from Metglas 2826MB, careful consideration is required for the placement of the driving teeth. The number of driving teeth is usually the same as the number of antinodes in the desired mode shape for a resonant rotary motor [9]. The driving teeth are typically offset from the location of the antinodes in order to ensure elliptical motion of the tooth tip. However, the mass loading added by the driving teeth causes the antinodes to shift to the same location as the teeth. Consequently, the teeth no longer move elliptically, and no rotation is generated. Therefore, as shown in Fig. 2(b), a design employing eight teeth is proposed to address the issue. There are still four sets of teeth, but one set of teeth is a combination of two teeth: an auxiliary tooth and a driving tooth, each separated slightly from each other. The auxiliary teeth and driving teeth have the same mass so that the mass center and antinodes of the vibratory mode shape will be in the center between the two different teeth. However, the driving tooth is taller, so only it will contact the rotor. As a result, the driving teeth can move in an elliptical manner and can drive the rotor tangentially.

The FEA results shown in Fig. 3 predict that a stator (4 mm inner diameter, 8 mm outer diameter, and 25 μm thickness) has the desired mode shape at a resonant frequency of about 11.43 kHz, with 0.1- μm out-of-plane deformation under harmonic excitation with an amplitude of 2 Oe. Due to the orientation and size of the teeth and spring suspension, a slightly different performance is predicted for different directions of alternating magnetic excitation. Simulation results suggest that applying magnetic field between the suspension springs gives the largest out-of-plane displacement amplitude. As desired, the vibration mode shape demonstrates that the antinodes are located in the center between a driving tooth and an auxiliary tooth.

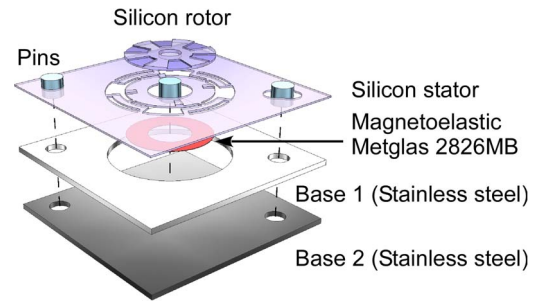


Fig. 4. Schematic of design S geometry. In design S, the stator is fabricated from a layer of magnetoelastic metal foil bonded to Si.

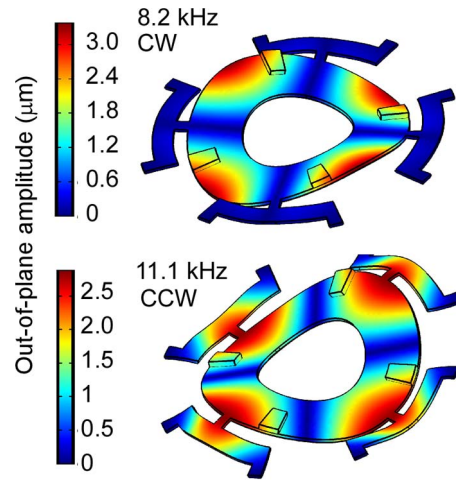


Fig. 5. FEA simulation results of the frequency response of the design M stator with two mode shapes.

D. Design S

As shown in Fig. 4, design S has a stacked structure similar to that of design M, but the stator is made of a silicon–Metglas sandwich instead of solely Metglas 2826MB. The benefit of silicon is that it has better surface uniformity compared to magnetoelastic foil. Furthermore, the higher resonant frequency and quality factor of the thicker silicon can potentially increase the rotation rate and can improve the positioning resolution. Using standard micromachining processes, silicon should facilitate the direct integration of the driving teeth on the stator. The thicker silicon also means that no auxiliary teeth are required in this design, and the intended bidirectional rotation can be realized by switching the driving frequency and mode shapes. A ring-shaped Metglas 2826MB disc is attached to the design S stator so that the motor is still wirelessly driven by magnetic fields. The rotor is patterned to have six radial segments so that the rotation rate can be measured visually or optically.

The FEA simulation results show that the design of the teeth can be simplified because the stator is thick and robust compared to the teeth. Additionally, bidirectional rotation can be achieved by switching the mode shapes of the stator (Fig. 5). The intended clockwise (CW) vibration mode shape of a design S stator with 4 mm inner diameter, 8 mm outer diameter, and 65 μm thickness is simulated to be at 8 kHz with 3.2- μm amplitude; the counterclockwise (CCW) vibration mode shape exists at 11 kHz with 2.7- μm out-of-plane amplitude. A 6-Oe magnitude ac magnetic field is applied in the simulation.

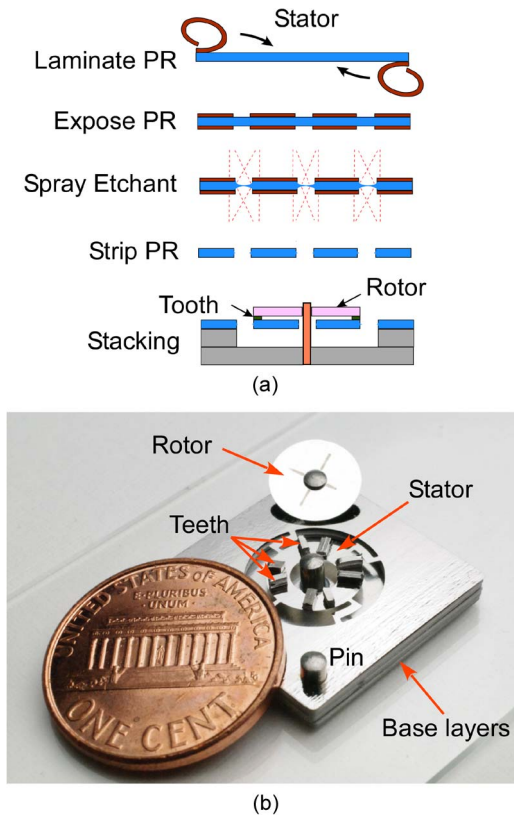


Fig. 6. (a) Fabrication process flow of design M. (b) Optical image of the assembled device.

E. Metglas 2826MB and Driving Methods

Metglas alloys provide excellent magnetostrictive properties as well as adequate mechanical properties. In this design, Metglas 2826MB, an amorphous NiFeMoB alloy, is used. Its saturation magnetostriction is 12 ppm, and its dc permeability is larger than 50 000 [20]. These materials are readily available in foils ($\approx 25 \mu\text{m}$ thick) and are easy to pattern by utilizing PCM. Relative to other Metglas alloys and magnetoelastic materials, 2826MB also requires a small dc bias (less than 10 Oe) and can be stimulated with a relatively small alternating field.

In principle, an onboard coil and permanent magnets can be implemented to provide the driving ac and dc magnetic fields. For example, inductive coils for generating ac magnetic fields can be patterned on an underlying silicon substrate using standard micromachining techniques. On the same substrate, permanent magnet materials such as permalloy or samarium cobalt can be deposited and used to provide the dc fields required to bias the magnetoelastic material. However, for the motors presented in this paper, external coils are used.

III. FABRICATION

The fabrication process flow of a design M motor is illustrated in Fig. 6(a). First, the magnetoelastic stator is batch-patterned using PCM [21] from the Metglas 2826MB foil. The ring-shaped stator is patterned with an inner diameter of 4 mm, an outer diameter of 8 mm, and a thickness of $25 \mu\text{m}$. Other base layers are also fabricated using PCM from 0.5-mm-thick

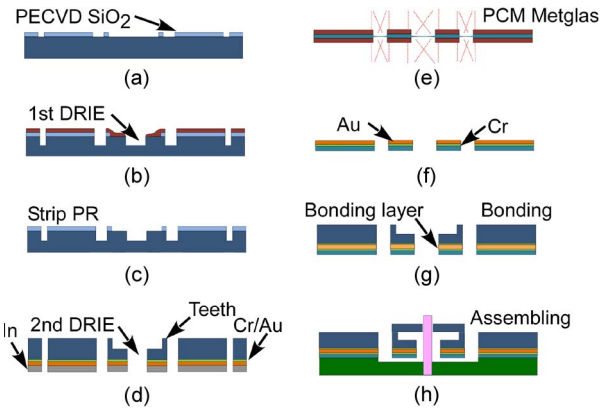


Fig. 7. Fabrication process flow of design M.

stainless steel foils. The layers are stacked and aligned with pins, and bonded to each other with epoxy. The stainless steel auxiliary teeth ($500 \mu\text{m}$ wide and $300 \mu\text{m}$ tall) and driving teeth ($300 \mu\text{m}$ wide and $500 \mu\text{m}$ tall) are manually placed on the stator and fixed with epoxy. The rotor is microelectrodischarge machined (μEDM) from Metglas 2826MB foil; it has a total mass of about 9 mg. A hub with a diameter of 2 mm is used to constrain the rotor. The overall size of the chip is $2 \times 2 \text{ cm}^2$ [Fig. 6(b)].

For design S, the stator and rotor are fabricated side by side using a two-mask deep reactive-ion etching (DRIE) process, as shown in Fig. 7(a)–(d). The fabrication process starts with coating a layer of KMPR 1010 on the backside of a silicon wafer, to serve as an etch stop and support layer for through-wafer etching. Silicon oxide of $4 \mu\text{m}$ thickness is then deposited on the front side of the wafer by PECVD and is patterned using mask 1. The silicon oxide layer is wet etched in 5 : 1 buffered hydrofluoric acid solution. Photoresist is used to make the first DRIE step in which the ring-shaped stator is defined. Then, the PR is removed, and the remaining silicon oxide layer is used to etch through the remainder of the wafer. At the end of this process, the ring-shaped stator is fully etched out along with the teeth that are located on the stator. After removing KMPR 1010 by immersing the wafer in Remover PG (MicroChem Corporation, Newton, MA, USA) at $80 \text{ }^\circ\text{C}$ for 1 h, the silicon rotor is ready for assembling. The silicon stator must be bonded to Metglas 2826MB as described in the following steps.

Silicon–Metglas 2826MB bonding is an important step because it affects the actuation of the silicon stator. An Au–In liquid transient phase bonding (TLP) is used because it can be performed at relatively low temperature, ensuring that magnetic properties of Metglas 2826MB will not change. Additionally, gold and indium can be easily coated using standard microfabrication steps. The possible stages of TLP bonding for indium rich are shown in Fig. 8 [22], [23]. Liquid–solid interdiffusion, stage 1, occurs when two substrates are brought into intimate contact while the temperature is above $157 \text{ }^\circ\text{C}$, and the appropriate pressure is applied. Liquid indium dissolves gold layers on both the silicon substrate and the Metglas 2826MB substrate. Simultaneously, dissolved gold diffuses into the indium layer to form AuIn^2 . Stage 2 occurs upon cooling; the final bonding

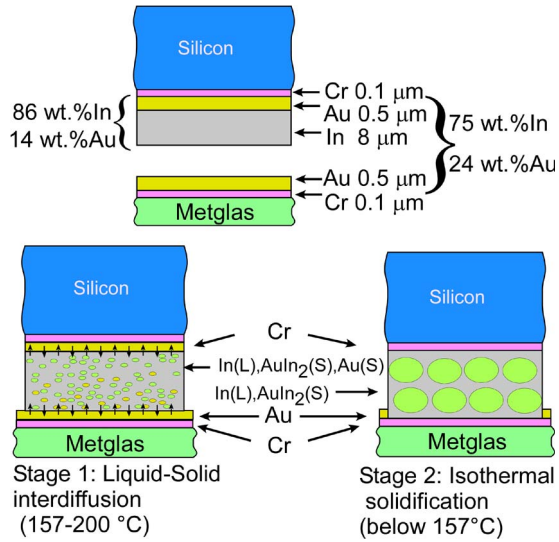


Fig. 8. Composition of Au-In TLP bonding and possible stages of the bonding process: stage 1, melting of In and liquid–solid interdiffusion at 157 °C–200 °C; stage 2, solidification of the mixture below 157 °C [22], [23].

layer is a mixture of solid indium and AuIn² because the quantity of gold is insufficient to react with all indium.

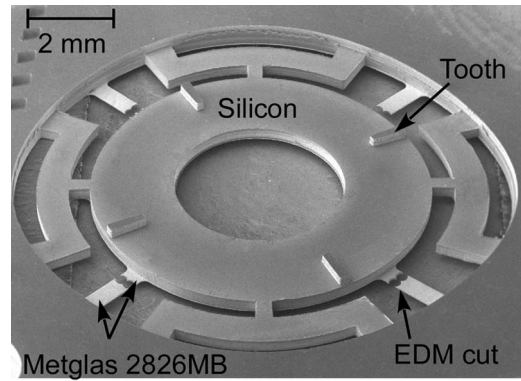
The use of this bonding step with the process sequence of the design S motors is shown in Fig. 7(d)–(g). Initially, chrome (0.1 μm) and gold (0.5 μm) are evaporated on both the Metglas 2826MB ring-shaped structure and the backside of the silicon stator. The step is followed by electroplating of ≈8-μm indium on the backside of the silicon stator. The silicon stator and the Metglas 2826MB component are aligned and bonded. The bonding process is performed in a vacuum oven so that oxidation is prevented. The temperature is held at 200 °C for 1 h during this step. After bonding, the connections between ring-shaped disc and frame in the Metglas 2826MB layer are cut using μEDM. An SEM image of the silicon stator with bonded ring-shaped Metglas 2826MB is shown in Fig. 9(a).

As the final step before testing, the design S stator, stainless steel bases, and a hub are aligned, stacked, and fixed to each other with epoxy. The silicon rotor located directly above the stator is constrained by hub and touches the stator only at the teeth. The optical image of the assembled design S motor is shown in Fig. 9(b).

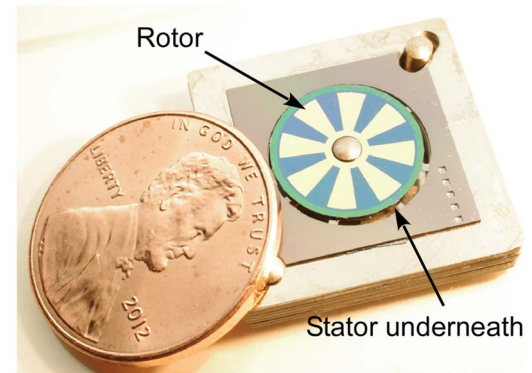
IV. EXPERIMENTAL METHODS AND RESULTS

A. Experimental Methods

The motors were actuated wirelessly using two sets of coils. Two coils with a diameter of 12.5 cm, shown in Fig. 10, were connected to a dc power supply providing constant current to provide a dc magnetic field. This arrangement was used to bias the magnetoelastic material into an operating region in which the strain is sensitive to magnetic field. For design M, based on the relationship between the magnetostriction coefficient and the applied field for Metglas 2826MB [24], the dc bias field was set to 3 Oe, with ±2-Oe ac field (Fig. 11). However, the effective magnetostriction curve appears to be shifted for design S, as suggested by the magnetic bias at which the rotation rate is highest. The cause of bias shift for design S may be related to residual stresses from the bonding process; the reference curve



(a)



(b)

Fig. 9. (a) SEM image of the design S stator. (b) Optical image of the assembled device (b).

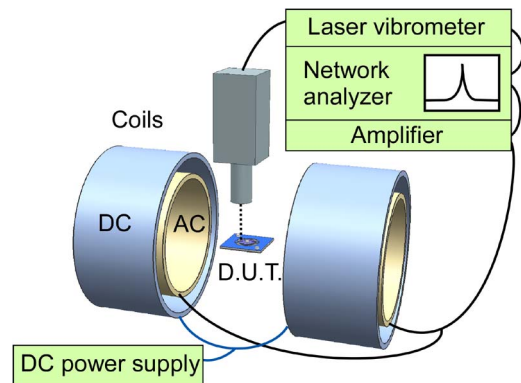


Fig. 10. Experimental set up for motor actuation and frequency response measurement.

was measured on a free–free sample. Thus, the dc bias field of design S was set to 8 Oe to achieve a high rotation rate.

Another two coils with a diameter of 11.5 cm were placed inside the dc coils; these smaller coils generated an alternating magnetic field with amplitude from 2 to 6 Oe. A dc current, equal to the measured ac current amplitude, was first applied on the ac coils. Subsequently, the dc magnetic field, equivalent to the ac magnetic field amplitude, was experimentally measured by an FW Bell 5180 Hall Effect Gaussmeter (Pacific Scientific OECO, Milwaukie, OR, USA). The device under test was placed between the coils.

To measure the frequency response of the stator, a laser vibrometer and a network analyzer were used in conjunction (Fig. 10). The vibration mode shape can be determined by

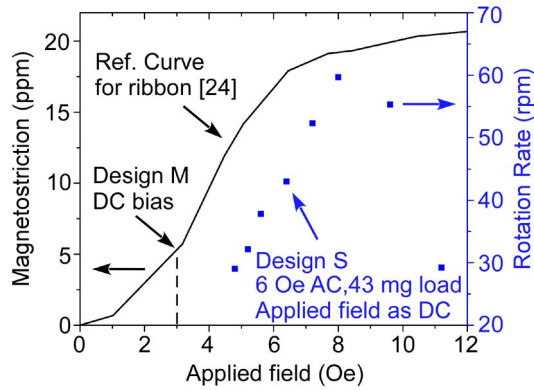


Fig. 11. Magnetostriction versus applied field for Metglas 2826MB (reproduced from [24]) and rotation rate versus applied dc bias at fixed ac field. The derivative of the reference curve at a bias point leads to the magnetostrictivity (“ d ”) in the constitutive equations in Section II-B at that bias point. The effective magnetostrictivity curve appears to be shifted for design S, as suggested by the magnetic bias at which the rotation rate is highest.

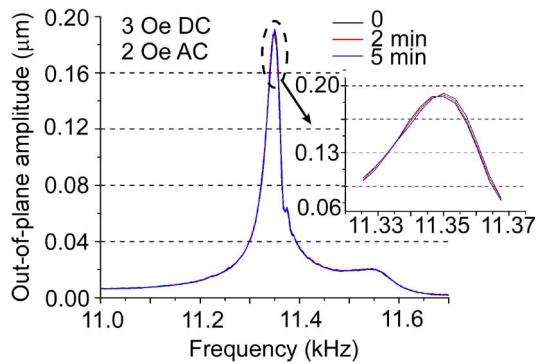


Fig. 12. Experimentally measured frequency response of bulk-magnetoelastic-foil stator of design M, with 3-Oe dc and 2-Oe amplitude ac magnetic fields.

measuring a number of points along the rim of the stator; antinodes of a given mode shape exist at locations of strong response at a given frequency.

A video camera was used to record the motors from above, and the video is analyzed frame by frame to derive the rotation rate and initial acceleration. In addition to this method, a laser displacement sensor was used to monitor the patterned surface of the rotor. The frequency of the resulting square wave was used to calculate the rotation rate.

B. Design M Results

The desired mode shape with four antinodes was confirmed to exist at 11.35 kHz, with 0.2- μm unloaded out-of-plane deflection at the antinodes. As shown in Fig. 12, the frequency response is stable over at least 5 min of operation time. In preliminary tests, a typical rotation rate of approximately 44 r/min (4.6 rad/s) was obtained (Fig. 13). An angular driving step size of about 23 mdeg is calculated from the measured angular velocity and resonant frequency. The angular velocities from different trials were calculated from the recordings and are shown in Fig. 14.

The associated start torque (i.e., the motor driving torque minus friction torque when rotation rate is approximately zero)

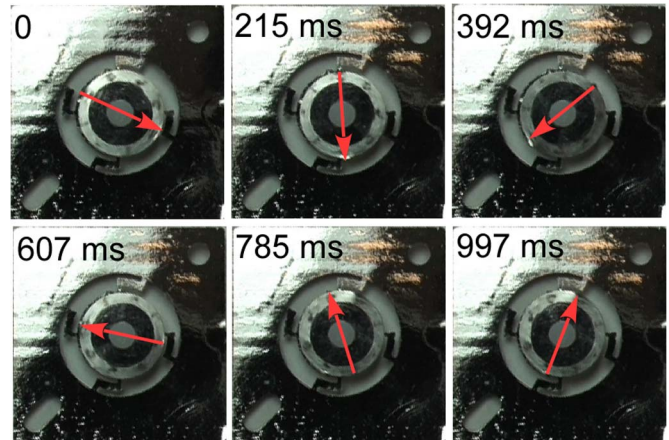


Fig. 13. Optical images of design M rotating with 3-Oe dc and 2-Oe amplitude ac magnetic fields at a frequency of 11.35 kHz and 9-mg payload.

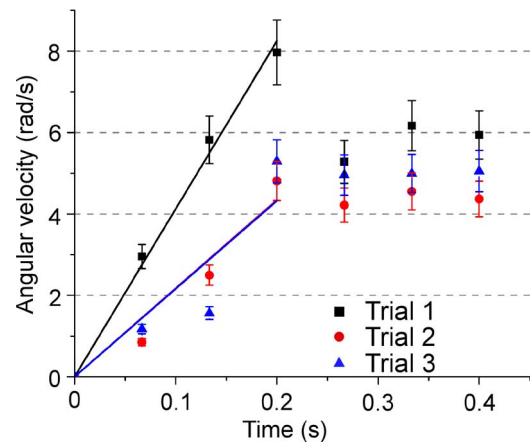


Fig. 14. Experimentally measured angular velocity of design M as a function of time with 3-Oe dc and 2-Oe amplitude ac magnetic fields at a frequency of 11.35 kHz. Linear fits of different trials were used to calculate initial acceleration.

is $\approx 2 \text{ nN} \cdot \text{m}$. This is calculated by $\tau = \alpha I$, where τ is the start torque and α is the angular acceleration. The angular acceleration, before the angular velocity plateaus, was derived from the average of linear fit slopes from different trials. The moment of inertia I is further given by $I = (1/2)m(r_1^2 + r_2^2)$, where m is the mass of the rotor and r_1 and r_2 are the inner and outer radii of the rotor, respectively.

C. Design S Results

The frequency response of design S was also measured, and it was confirmed that two mode shapes exist that can provide bidirectional operation. The CW mode shape was confirmed to exist at 6.08 kHz, with about 2- μm unloaded out-of-plane deflection at the antinodes [Fig. 15(a)], whereas the CCW mode shape was confirmed to exist at 7.85 kHz, with about 1.8- μm unloaded out-of-plane deflection at the antinodes [Fig. 15(b)]. The frequencies are lower than the FEA results. Further study is required to understand the reason for the lower-than-expected resonant frequency.

The bidirectional rotation was demonstrated at corresponding resonant frequencies. The typical rotation rates of CW and

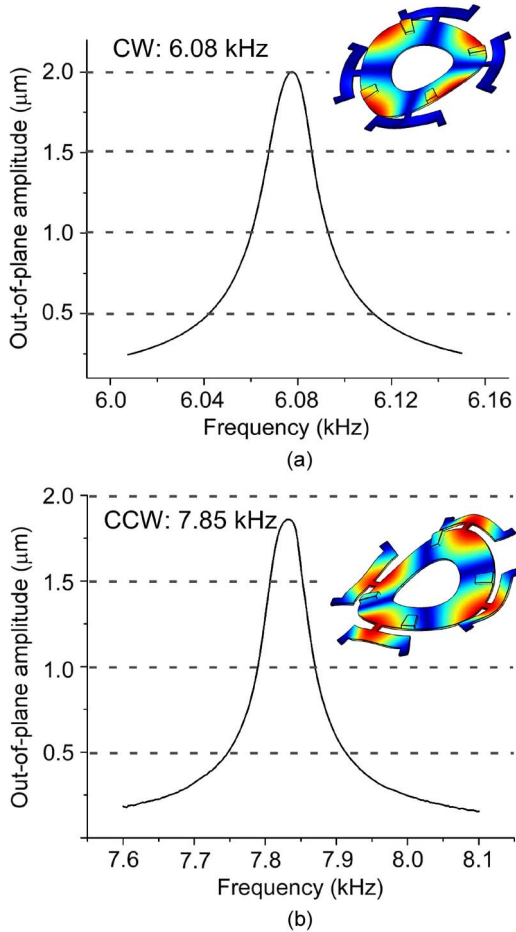


Fig. 15. Experimentally measured frequency response of design S stator with no load.

CCW directions are about 30 and 100 r/min when an 22-mg rotor was used and an ac magnetic field with about 6-Oe amplitude and a dc magnetic field with 8-Oe amplitude were applied. However, the CW rotation rate is relatively slow, and rotor wobbling was observed. This is possibly due to the tooth locations that are too close to the antinodes of CW vibration mode shape. Consequently, vertical movement, instead of tangential movement, dominates the motion of the tooth tip so that the rotor is mainly pushed up and down rather than tangentially. This problem can be solved by placing the tooth equally far from the antinodes of both CW and CCW mode shapes in future designs. More characterization was performed on the CCW mode.

The effect of payload on CCW rotation rate was characterized by using rotors with different weights. For example, for the 43-mg rotor with six patterned segments used in this test, a square wave was obtained to calculate the rotation rate of about 60 r/min (Fig. 16). As shown in Fig. 17, the rotation rate decreases when the payload increases in an approximate linear relationship. Design S showed at least 43-mg payload capability. The rotation rate was also closely related to applied power or applied ac magnetic field strength. The rotation rates were measured when the magnitude of the ac magnetic field increases from 3 to 6 Oe. As shown in Fig. 18, rotation rate increases with the increasing ac magnetic field in an ap-

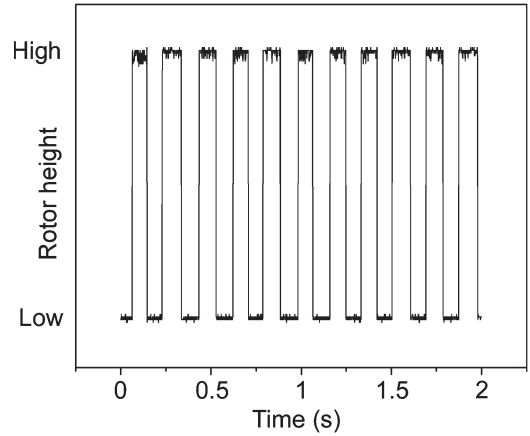


Fig. 16. Rotation rate measurement of design S with 43-mg payload and 8-Oe dc and 6-Oe amplitude ac magnetic fields at a frequency of 7.85 kHz.

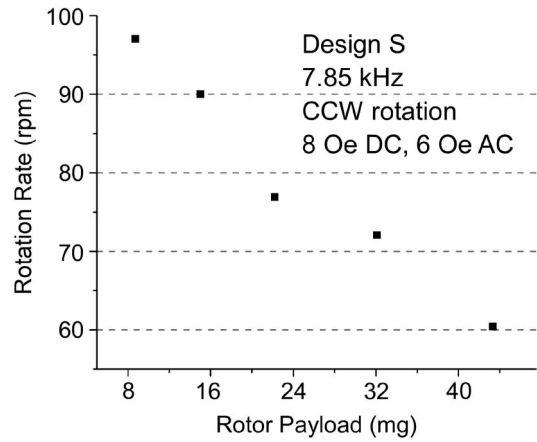


Fig. 17. Experimentally obtained effect of payload on rotation rate of design S, with 8-Oe dc and 6-Oe amplitude ac magnetic fields at a frequency of 7.85 kHz.

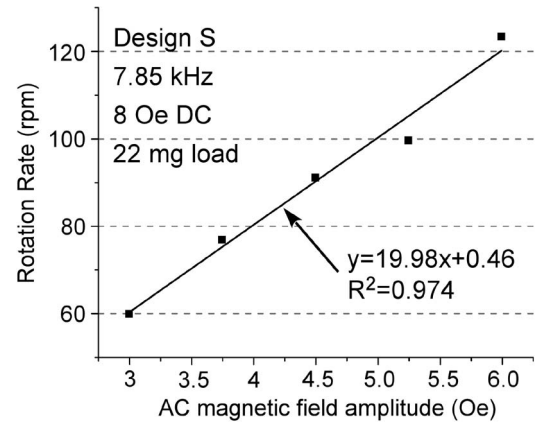


Fig. 18. Experimentally obtained effect of applied ac magnetic field on rotation rate of design S, with 8-Oe dc, with 22-mg payload, and at a frequency of 7.85 kHz.

proximately linear manner. This indicates that magnetoelastic material still operates in the intended linear region of magnetostriction versus applied field curve.

The transient response of design S was experimentally evaluated. The results obtained with a 22-mg payload are shown in Fig. 19. These data were obtained by analyzing a slow-motion video. The typical performance achieved a rotation rate of about 100 r/min, start torque of 30 nN · m, and step size of 74 mdeg.

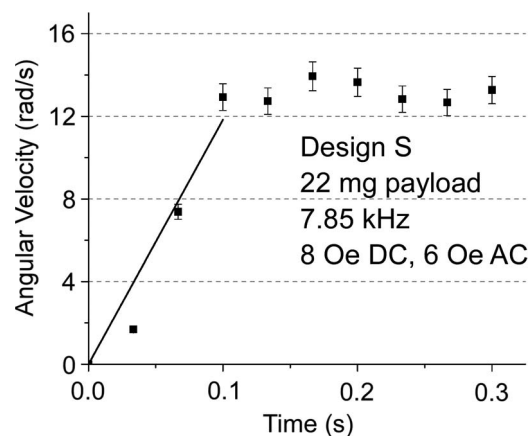


Fig. 19. Experimentally measured angular velocity of design S as a function of time with 8-Oe dc and 6-Oe amplitude ac magnetic fields, a frequency of 7.85 kHz, and a 22-mg payload. Linear fit was used to calculate initial acceleration.

TABLE I
TYPICAL ROTATION RATE, DRIVING STEP SIZE, START TORQUE,
PAYLOAD, AND BIDIRECTIONAL ROTATION CAPABILITY
OF DESIGN M AND DESIGN S

	Design M	Design S
Rotation rate (rpm)	44	100
Step size (milli-degree)	23	74
Start torque (n·Nm)	2	30
Payload (mg)	9	43
Bi-directional	No	Yes

The start torque is calculated using the same method for design M.

The performance of the two designs is summarized and compared in Table I.

V. DISCUSSION

The magnetoelastic wireless resonant motors demonstrate that the magnetoelastic material has significant potential for actuation in miniature and microscale devices. The main advantage—the wireless aspect of the actuation approach—allows miniaturization and eliminates lead transfer actuator, which is especially preferred for implantable applications. Along with being wireless, magnetoelastic resonant motors offer the advantages of ultrasonic piezoelectric motors, such as high precision. Design S was able to move at least a 43-mg payload. These capabilities will enable integration of inertial sensors on the rotor in the future.

Design M demonstrated the concept of wireless magnetoelastic actuation, but the performance was compromised by two factors. First, the positioning and assembling of the teeth, which was performed manually, contributed to a loss of performance. Second, an uneven magnetoelastic stator surface resulted in unstable rotation rate. Furthermore, because the customized teeth design limits vibration mode shapes of the stator, only CW rotation was achieved. Design S was designed based on the results of design M. The thick silicon stator has better surface uniformity and simplifies the tooth design. This resulted in stable rotation rate and bidirectional operation capability. Design M also exhibited a larger payload capability. The Au–In TLP bonding process was customized to attach magnetoelastic

material to silicon. This bonding process has potential applications in other magnetoelastic actuation and sensing systems.

Although integration of the actuation coil with the stator chip is beyond the scope of the present effort, it is worthwhile to consider what options exist for generating the magnetic field on-chip. Utilizing FEA simulations similar to those described in Section II, the power consumption for design S can be estimated. The power required to achieve the necessary magnetic field with small coils placed in close proximity to the motor is about 74 mW. A rectangular copper sheet located 50 μm beneath the magnetoelastic stator carrying 150 mA, together with a permanent magnetic providing the dc field, should be sufficient to achieve actuation. In contrast, long-distance wireless control can be realized by compromising the performance or power efficiency. For example, if utilizing an experimental setup similar to that in this paper, an ac current of 5-A amplitude provides a 6-Oe amplitude ac magnetic field with a 50-turns Helmholtz coil of 40-cm radius (which is equivalent to the wireless distance). A power amplifier is necessary in this case. In general, the wireless control distance is determined by performance requirement, power budget, and other factors, on a case-by-case basis.

Compared to conventional electromagnetic motors, magnetoelastic micromotors have very simple structures and only require a single ac excitation signal. The performance of rotation rate and step size can be potentially improved by increasing the resonant frequency of the silicon stator. This can be achieved by either increasing the thickness of the stator or decreasing the size of the stator. Additionally, a method for braking the motion of the rotor can be provided by exploiting bidirectional rotation capability. For example, CCW rotation can be stopped abruptly by switching the exciting frequency from CCW to CW with a calibrated ac magnetic field. Finally, as mentioned before, external coils can be potentially replaced by on-chip driving coils for short-range wireless operation.

VI. CONCLUSION

This paper has presented the analysis, fabrication, and experimental results for two types of magnetoelastically actuated chip-scale rotary motors. Both designs were successfully wirelessly actuated using external coils. For design M, a new approach that employs auxiliary teeth and driving teeth was used to customize the resonant behavior of the stator. A stator of $\phi 8$ mm diameter, fabricated from 25- μm -thick magnetoelastic foil typically achieved a rotation rate of about 44 r/min, angular driving step size of about 23 mdeg, and payload of 9 mg. Design S used a stator that is a sandwich of Si (65 μm thick) and magnetoelastic foil (25 μm thick). An Au–In TLP bonding process was used to bond bulk-magnetoelastic-foil to the silicon stator. Bidirectional rotation was realized by switching the applied frequency and exciting at a slightly different mode shape. The typical performance achieved by an 8-mm-diameter stator with a 22-mg payload was a rotation rate of about 100 r/min, start torque of 30 nN·m, and driving step size of 74 mdeg. Design S also showed at least 43-mg payload capability. Future efforts will be directed at increasing the rotation rate, improving the angular resolution, and integrating driving and control circuits.

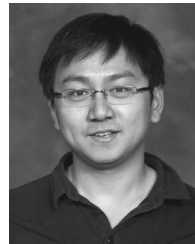
In the long term, such motors can be potentially used in calibrating microgyroscopes or for robotic navigation in tubes or pipes.

ACKNOWLEDGMENT

The authors would like to thank Prof. K. Grosh from the Department of Mechanical Engineering, University of Michigan, Ann Arbor, MI, USA, for providing access to a laser vibrometer used in testing, and Metglas, Inc., for the samples provided for this paper.

REFERENCES

- [1] Y.-C. Tai, L.-S. Fan, and R. S. Muller, "IC-processed electrostatic micromotors," *Sens. Actuators A, Phys.*, vol. 20, no. 1/2, pp. 41–47, Nov. 1989.
- [2] L.-S. Fan, Y.-C. Tai, and R. S. Muller, "IC-processed micro-motors: Design, technology, and testing," in *Proc. IEEE Investigation Micro Struct., Sens., Actuators, Mach. Robots Micro Electro Mech. Syst.*, 1989, pp. 1–6.
- [3] N. Ghalichechian, A. Modafe, M. I. Beyaz, and R. Ghodssi, "Design, fabrication, and characterization of a rotary micromotor supported on microball bearings," *J. Microelectromech. Syst.*, vol. 17, no. 3, pp. 632–642, Jun. 2008.
- [4] G. Sun, T. Liu, P. Sen, W. Shen, C. Gudeman, and C.-J. Kim, "Electrostatically driven rotor on conductive liquid ring bearings," in *Proc. Solid-State Sens., Actuators, Microsyst. Workshop*, Hilton Head Island, SC, USA, 2012, pp. 78–81.
- [5] H. Guckel, K. J. Skrobis, T. R. Christenson, J. Klein, S. Han, B. Choi, E. G. Lovell, and T. W. Chapman, "Fabrication and testing of the planar magnetic micromotor," *J. Micromech. Microeng.*, vol. 1, no. 4, pp. 135–138, Sep. 1991.
- [6] H. Guckel, T. R. Christenson, K. J. Skrobis, T. S. Jung, J. Klein, K. V. Hartojo, and I. Widjaja, "A first functional current excited planar rotational magnetic micromotor," in *Proc. IEEE Int. Conf. Micro Electro Mech. Syst.*, 1993, pp. 7–11.
- [7] C. H. Ahn, Y. J. Kim, and M. G. Allen, "A planar variable reluctance magnetic micromotor with fully integrated stator and coils," *J. Microelectromech. Syst.*, vol. 2, no. 4, pp. 165–173, Dec. 1993.
- [8] D. P. Arnold, S. Das, F. Cros, I. Zana, M. G. Allen, and J. H. Lang, "Magnetic induction machines integrated into bulk-micromachined silicon," *J. Microelectromech. Syst.*, vol. 15, no. 2, pp. 406–414, Apr. 2006.
- [9] A. Iino, K. Suzuki, M. Kasuga, M. Suzuki, and T. Yamanaka, "Development of a self-oscillating ultrasonic micro-motor and its application to a watch," *Ultrasonics*, vol. 38, no. 1–8, pp. 54–59, Mar. 2000.
- [10] T. Kanda, A. Makino, T. Ono, K. Suzumori, T. Morita, and M. K. Kurosawa, "A micro ultrasonic motor using a micro-machined cylindrical bulk PZT transducer," *Sens. Actuators A, Phys.*, vol. 127, no. 1, pp. 131–138, Feb. 2006.
- [11] V. Kaajakari and A. Lal, "Micromachined ultrasonic motor based on parametric polycrystalline silicon plate excitation," *Sens. Actuators A, Phys.*, vol. 137, no. 1, pp. 120–128, Jun. 2007.
- [12] B. Watson, J. Friend, and L. Yeo, "Piezoelectric ultrasonic micro/mill-scale actuators," *Sens. Actuators A, Phys.*, vol. 152, no. 2, pp. 219–233, Jun. 2009.
- [13] Z. Qi, P. C. Liang, M. Y. Ting, K. F. Rang, and F. Z. Hua, "Piezoelectric rotary motor based on active bulk torsional element with grooved helical electrodes," *IEEE/ASME Trans. Mechatronics*, vol. 17, no. 2, pp. 260–268, Apr. 2012.
- [14] S. Piratla, M. Pandey, and A. Lal, "Nanogap ultrasonic actuator for non-contact control of levitated inertial sensor rotor," in *Proc. Solid-State Sens., Actuators, Microsyst. Workshop*, Hilton Head Island, SC, USA, 2012, pp. 82–85.
- [15] J. S. Park, L. L. Chu, A. D. Oliver, and Y. B. Gianchandani, "Bent-beam electrothermal actuators—Part II: Linear and rotary microengines," *J. Microelectromech. Syst.*, vol. 10, no. 2, pp. 255–262, Jun. 2001.
- [16] C. A. Grimes, S. C. Roy, S. Rani, and Q. Y. Cai, "Theory, instrumentation and applications of magnetoelastic resonance sensors: A review," *Sensors*, vol. 11, no. 3, pp. 2809–2844, Mar. 2011.
- [17] J. Tang, S. R. Green, and Y. B. Gianchandani, "Miniature wireless resonant rotary motor actuated by lithographically micromachined magnetoelastic foil," in *Proc. Solid-State Sens., Actuators, Microsyst. Workshop*, Hilton Head Island, SC, USA, 2012, pp. 86–89.
- [18] S. R. Green and Y. B. Gianchandani, "Wireless magnetoelastic monitoring of biliary stents," *J. Microelectromech. Syst.*, vol. 18, no. 1, pp. 64–78, Feb. 2009.
- [19] J. Benatar, "FEM implementations of magnetostrictive-based applications," M.S. thesis, Dept. Aerosp. Eng., Univ. Maryland, College Park, MD, USA, 2005.
- [20] Metglas, Inc. (2003). Magnetic Alloy 2826MB (Nickel-Based) Technical Bulletin, Conway, SC, USA. [Online]. Available: <http://www.metglas.com>
- [21] *ASM Handbook*, vol. 16. Materials Park, OH, USA: ASM Int., 1989.
- [22] C. C. Lee, C. Y. Wang, and G. Matijasevic, "Au–In bonding below the eutectic temperature," *IEEE Trans. Compon. Hybrids Manuf. Technol.*, vol. 16, no. 3, pp. 311–316, May 1993.
- [23] W. W. So and C. C. Lee, "Fluxless process of fabricating In–Au joints on copper substrates," *IEEE Trans. Compon. Packag. Technol.*, vol. 23, no. 2, pp. 377–382, Jun. 2000.
- [24] M. Hyoung Kim, K. Shik Lee, and S. Ho Lim, "Magnetostriction measurements of metallic glass ribbon by fiber-optic Mach–Zehnder interferometry," *J. Magn. Magn. Mater.*, vol. 191, no. 1, pp. 107–112, Jan. 1999.



Jun Tang received the B.S. degree in electronic science and technology from Huazhong University of Science and Technology, Wuhan, China, in 2007 and the M.S. degree in microelectronics and solid-state electronics from Shanghai Jiao Tong University, Shanghai, China, in 2010. He is currently working toward the Ph.D. degree in the Department of Mechanical Engineering, University of Michigan, Ann Arbor, MI, USA, with a focus on microelectromechanical systems.

He is currently a Graduate Student Research Assistant with the Department of Mechanical Engineering, University of Michigan. His research interests include wireless magnetoelastic sensors and actuators.



Scott R. Green received the B.S. degree in mechanical engineering from Rose–Hulman Institute of Technology, Terre Haute, IN, USA, in 2003 and the M.S. and Ph.D. degrees in mechanical engineering from the University of Michigan, Ann Arbor, MI, USA, with a focus on microelectromechanical systems.

He was a Senior Design Engineer with the Instruments Division, Stryker Corporation, from 2003 to 2005, developing minimally invasive surgical devices for vertebroplasty and discectomy procedures. He is currently an Assistant Research Scientist with the University of Michigan. His research interests include wireless magnetoelastic sensors and actuators, miniature implantable medical systems, and miniature and microfabricated high-vacuum sputter ion pumps.



Yogesh B. Gianchandani (S'83–M'85–SM'05–F'10) received the B.S. degree in electrical engineering from the University of California, Irvine, CA, USA, in 1984, the M.S. degree in electrical engineering from the University of California, Los Angeles, CA, USA, in 1986, and the Ph.D. degree in electrical engineering from the University of Michigan, Ann Arbor, MI, USA, in 1994.

He is currently a Professor with the University of Michigan with a primary appointment in the Department of Electrical Engineering and Computer Science and a courtesy appointment in the Department of Mechanical Engineering. He also serves as the Director of the Center for Wireless Integrated MicroSensing and Systems (WIMS²). He has published more than 250 papers in journals and conference proceedings and has about 35 U.S. patents issued or pending. He was a Chief Coeditor of *Comprehensive Microsystems: Fundamentals, Technology, and Applications*, published in 2008. He serves several journals as an Editor or a Member of the Editorial Board. His research interests include all aspects of design, fabrication, and packaging of micromachined sensors and actuators and their interface circuits.

Dr. Gianchandani served as the General Cochair for the IEEE/ASME International Conference on Microelectromechanical Systems in 2002. From 2007 to 2009, he also served at the National Science Foundation as the Program Director for Micro and Nano Systems within the Electrical, Communication, and Cyber Systems Division.